PHYSICAL REVIEW B VOLUME 61, NUMBER 13 1 APRIL 2000-I

Electron diffraction studies of phonon and static disorder in $SrTiO_3$

Renhui Wang
Department of Applied Science, Brookhaven National Laboratory, Upton, New York 11973
and Department of Physics, Wuhan University, Wuhan 430 072, China

Yimei Zhu*
Department of Applied Science, Brookhaven National Laboratory, Upton, New York 11973

S. M. Shapiro
Department of Physics, Brookhaven National Laboratory, Upton, New York 11973

(Received 16 July 1999; revised manuscript received 5 November 1999)

Three kinds of diffuse scattering associated with phonon and static disorder in $SrTiO_3$ were studied by electron diffraction with a parallel beam. (1) Streaks of diffuse scattering along the reciprocal lines MRM were found to originate from dynamically correlated rotations of oxygen-octahedra within the (0 0 1) layer and uncorrelated rotation between the layers; when temperature is lowered to the transition temperature $T_c \cong 103\,\mathrm{K}$, the crystal structure condenses into thin plates of antiphase domains in every orientational variant. (2) Diffuse scattering around the R point, due to the Γ_{25} phonon mode, becomes weaker and broader with an increase in temperature and is even detectable at 700 K. (3) Sheets of diffuse scattering in the reciprocal X-Γ-X-M-X plane result from the correlated movements of atomic chains along the [0 0 1] direction. Structural models are proposed to interpret these diffuse scatterings.

I. INTRODUCTION

The cubic-to-tetragonal phase transition in strontium titanate, $SrTiO_3$, has been studied extensively[1–8] because of its importance in understanding the fundamental physics associated with phase transitions in materials. Cubic $SrTiO_3$ possesses a typical perovskite structure of space group of $Pm\overline{3}m$ with a lattice constant $a_p = 0.3905\,\mathrm{nm}$ at room temperature (RT). Cubic perovskite may be described as consisting of corner-linked TiO_6 octahedra forming a three-dimensional framework. The strontium ions lie at the center of the eight neighboring octahedra. At the transition temperature $T_c \cong 103\,\mathrm{K}$, $SrTiO_3$ undergoes a structural phase transformation into a tetragonal low-temperature phase of space group $I4/mcm$ with $a = 0.5511\,\mathrm{nm} = \sqrt{2a_p}$ and $c = 0.7796\,\mathrm{nm} = 2a_p$. The low-temperature structure reflects a structural transition from the cubic perovskite by the rotation of all the octahedra around the tetragonal c axis, which is one of the $\langle 1\ 0\ 0\rangle$ axes of the prototypic perovskite; successive octahedra have opposite tilts.

Figure 1 shows a reciprocal unit-cell of the cubic $SrTiO_3$. Conventional symbols[7] are used, where Γ designates a reciprocal lattice point, and X, M, and R designate particular points at Brillouin zone boundaries along the $\langle 1\ 0\ 0\rangle^*$, $\langle 1\ 1\ 0\rangle^*$, and $\langle 1\ 1\ 1\rangle^*$ directions, respectively, with the Γ point being the zone origin.

Shirane and Yamada[1] showed that diffuse scattering around the R point is due to the Γ_{25} phonon mode. Its instability leads to the cubic-to-tetragonal phase transition of $SrTiO_3$ at $T_c \cong 103\,\mathrm{K}$. When $T < T_c$, the R points become superlattice points of the tetragonal $SrTiO_3$. Previous investigations[2–4] of diffuse scattering were carried out by neutron and x-ray probes. In general, neutron scattering experiments explore bulk properties at high energy resolution, and x rays confer high surface sensitivity and good momentum space resolution. Here, we report our investigations using an electron beam probing through the entire thickness of thin $SrTiO_3$ crystals, exploiting two advantages of electron diffraction in transmission electron microscopes (TEM): (a) The high sensitivity of electron diffraction in detecting weak diffuse scattering and (b) the flat Ewald-sphere that allowed us to record a large number of reflections simultaneously with one exposure in selected-area electron diffraction mode. As a result, we observed some phenomena in the diffuse scattering in $SrTiO_3$, which may be related to different types of soft phonons, static disorder, and domain structures in the crystal.

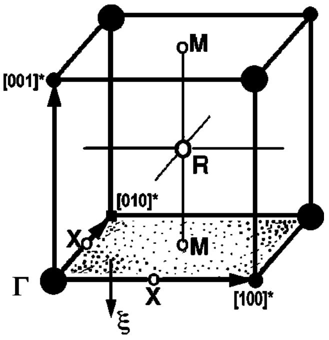

FIG. 1. The reciprocal unit cell of cubic $SrTiO_3$, showing the X, M, and R points at the Brillouin-zone boundaries along the $\langle 1\ 0\ 0\rangle^*$, $\langle 1\ 1\ 0\rangle^*$, and $\langle 1\ 1\ 1\rangle^*$ directions, respectively, with the Γ point being the zone origin. The observed diffuse scatterings are thermal diffuse-scattering around the Γ point, diffuse scattering around the R point, diffuse streaks along the MRM lines, and diffuse scattering of the sheets X-Γ-X-M-X, which are reciprocal $\{0\ 0\ 1\}^*$ planes passing through fundamental lattice points.

0163-1829/2000/61(13)/8814(9)/$15.00

II. EXPERIMENTAL

Single $SrTiO_3$ crystals of $15\,mm \times 15\,mm \times 0.5\,mm$ with a shiny flat (1 0 0) surface, supplied by Atomergic Chemetals Co., were previously studied by x-ray and neutron scattering.[5] Both planar (1 0 0) and cross-section (0 1 1) foils for TEM observation were prepared by a standard procedure, i.e., thin slices were cut using an abrasive slurry wire saw and an ultrasonic disc cutter, grounded to about 90 μm thick, and mechanically dimpled to about 25 μm at the center. The samples were ion-milled to perforation using a Gatan Model 600 Dual Ion Mill with 4 keV Ar ions and 1 mA beam current at decreased glancing angles from 16°, 12°, to 10°.

TEM observations were made with a JEOL 2000 FX microscope operated at 200 kV, and a JEOL 3000F FEG microscope operated at 300 kV; both are equipped with a heating or a cooling stage. The lowest nominal temperature for the cooling stage is about 20 and 89 K for liquid He and liquid N_2, respectively. For the quantitative analysis of electron diffraction, a Fuji Imaging Plate System and a Gatan Energy Filter with a CCD camera were used.

III. RESULTS

The standard space group of the low-temperature $SrTiO_3$ is $I4/mcm$. To conveniently compare the reflections of cubic and tetragonal $SrTiO_3$, a unit-cell of $2a_p \times 2a_p \times 2a_p$ was taken[6] for low-temperature $SrTiO_3$. In this case, the space group is $F4/mmc$ (see Ref. 9). Reflections $(h\;k\;l)$ with h, k, and l all even are fundamental reflections common to both the cubic and tetragonal $SrTiO_3$, while reflections $(h\;k\;l)$ with h, k, and l all odd are superlattice reflections, characteristic of tetragonal $SrTiO_3$. Moreover, the structure factors of the $(h\;k\;k)$ type reflections for orientational domain V_a, whose c axis is parallel to the [1 0 0] direction of the prototypic cubic perovskite, should be zero because of the c-glide plane. In the following, we designate all the $(h\;k\;l)$ superreflections with h, k, and l all odd as $(h\,k\,l)/2$ using the coordinate system of prototypic cubic perovskite.[1]

A. Diffuse scattering of ⟨1 0 0⟩* reciprocal rods passing through *R* points and superreflections

Figure 2 shows electron diffraction patterns (EDPs) along the [1 5 4] zone axis which deviates by 11° from the [0 1 1] towards the [1 2 1] axis. Figure 2(a) taken at 20 K, clearly shows streaking and splitting of the superreflections. For example, the superreflections $(5\,\bar{3}\,3)/2$, $(\bar{7}\,1\,1)/2$, $(\bar{1}\,\bar{5}\,7)/2$, $(7\,\bar{1}\,\bar{1})/2$, and $(9\,\bar{1}\,\bar{1})/2$ designated in the figure are split along the $[0\,1\,\bar{1}]^*$ direction. We note that the splitting distance of $(7\,\bar{1}\,\bar{1})/2$ is larger than that of $(9\,\bar{1}\,\bar{1})/2$, while $(11\,\bar{1}\,\bar{1})/2$ does not split. In some cases, we only observed one of the split spots; for example, the upper spot of the split $(3\,3\,\bar{5})/2$, and the lower spot of the split $(\bar{3}\,\bar{3}\,5)/2$. In Fig. 2(a), streaks along [1 0 0]* direction, e.g., the streak connecting $(5\,3\,\bar{5})/2$ and $(7\,3\,\bar{5})/2$, and the streak connecting $(\bar{3}\,\bar{5}\,7)/2$ and $(\bar{1}\,\bar{5}\,7)/2$ are rather sharp and their intensities are quite strong. The inset of Fig. 2(a) is an enlarged region of the boxed area, showing the details of the streak connecting spots $(\bar{3}\,\bar{5}\,7)/2$ and $(\bar{1}\,\bar{5}\,7)/2$, and the splitting of the spot $(\bar{1}\,\bar{5}\,7)/2$. However, there is neither a streak connecting $(7\,\bar{1}\,\bar{1})/2$, $(9\,\bar{1}\,\bar{1})/2$, and $(11\,\bar{1}\,\bar{1})/2$, nor one connecting $(\bar{9}\,1\,1)/2$ and $(\bar{7}\,1\,1)/2$.

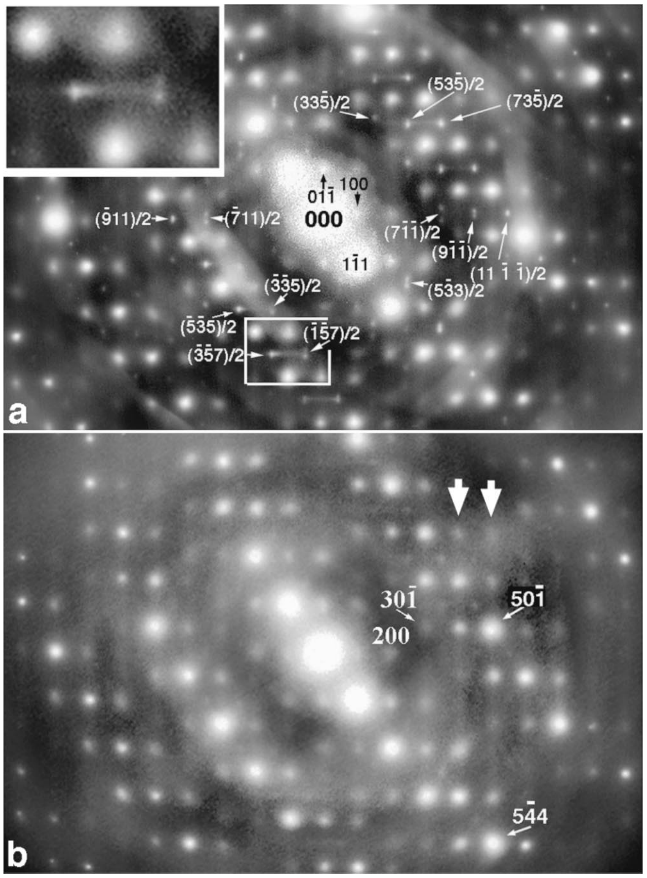

FIG. 2. EDPs of the [154] zone axis at two different temperatures. (a) 20 K, showing sharp streaking along the [1 0 0]* direction and splitting of the superreflections along the $[0\,1\,\bar{1}]^*$ direction. Inset is a boxed area showing details of the streak connecting spots $(\bar{3}\,\bar{5}\,7)/2$ and $(\bar{1}\,\bar{5}\,7)/2$, and splitting of the spot $(\bar{1}\,\bar{5}\,7)/2$; (b) 422 K, showing the intensity distribution of diffuse streaks (marked by vertical broad arrows) which are perpendicular to the [1 0 0] direction and pass through fundamental reflections.

The EDP shown in Fig. 3 was taken at 20 K and deviates by 2° from the [1 2 1] axis towards the [1 1 1] axis. In Fig. 3, streaks along the [1 0 0]* and [0 0 1]* direction are clearly visible, e.g., the streak from $(\bar{1}\,3\,\bar{5})/2$ pointing to $(13\bar{5})/2$, and the streak from $(\bar{1}\,3\,\bar{5})/2$ pointing to $(\bar{1}\,3\,\bar{3})/2$. A portion of Fig. 3 is shown in the inset.

Figure 4 is a set of EDPs with the same orientation, which deviate by 4°–5° from the [0 1 1] zone axis towards the [0 0 1] axis, showing the temperature-dependence of the diffuse scattering. In Fig. 4(a), taken at 24 K, there are streaks along the [1 0 0]* direction, e.g., the streak connecting superreflections $(\bar{1}\,9\,\bar{7})/2$ and $(1\,9\,\bar{7})/2$.

All the splitting and streaking behaviors shown in Figs. 2, 3, and 4 and those observed in other EDPs may be explained by considering a reciprocal rod passing through each superlattice point along the tetragonal $[0\,0\,1]_T$ direction. The axial ratio $c/\sqrt{2a}$ for tetragonal $SrTiO_3$ is very close to unity[1,8] ($c/\sqrt{2a} = 1.0003$ at 87 K and $c/\sqrt{2a} = 1.0006$ at 78 K). Hence, we cannot simultaneously observe all three spots

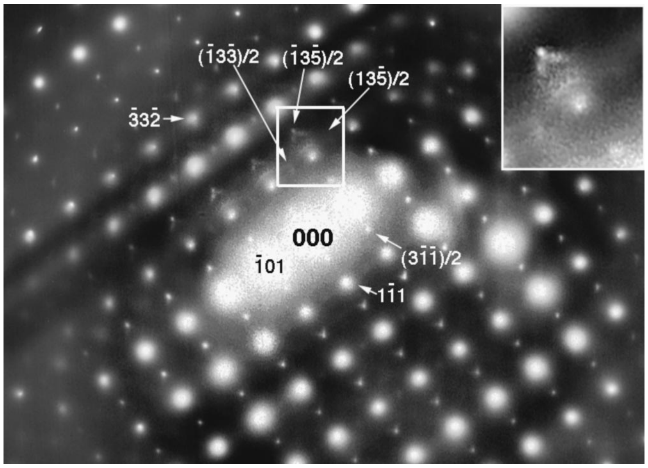

FIG. 3. EDP taken at 20 K, which deviates 2° from the $[1\ 2\ 1]$ axis towards the $[1\ 1\ 1]$ direction, showing streaks along $[1\ 0\ 0]^*$ and $[0\ 0\ 1]^*$. The inset is the enlarged pattern of the boxed area.

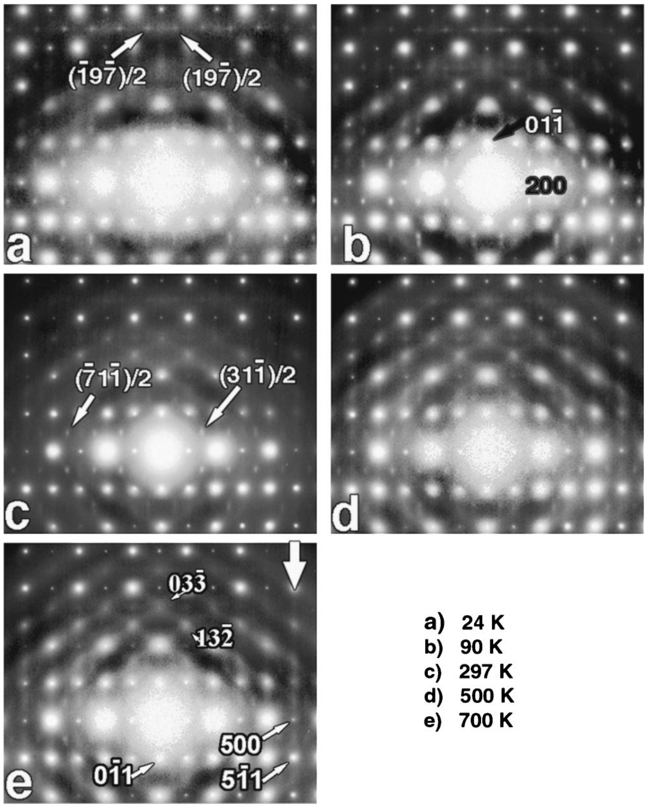

FIG. 4. A set of EDPs from the same crystal orientation which deviate by about 4°–5° from the $[0\ 1\ 1]$ zone axis towards the $[0\ 0\ 1]$ direction, showing the change of intensity of diffuse scattering with temperature. (a) 24 K; (b) 90 K; (c) 297 K; (d) 500 K; and (e) 700 K.

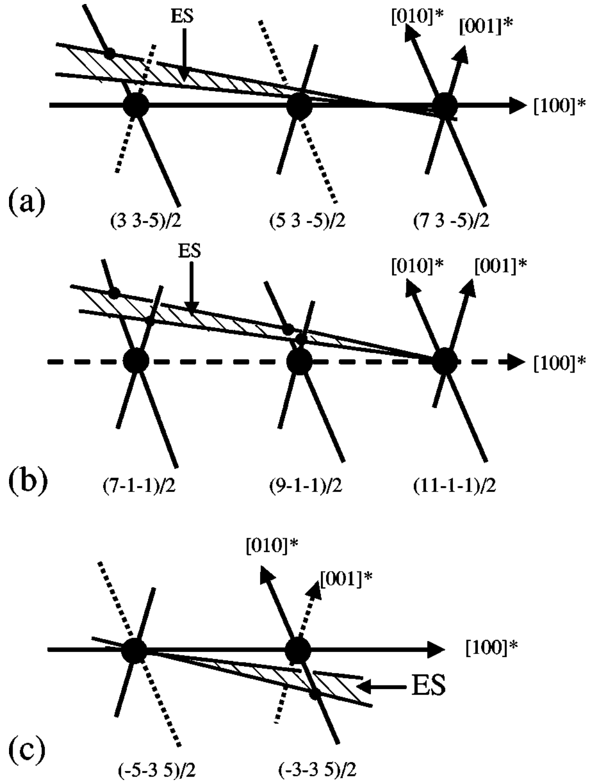

FIG. 5. Schematic diagrams showing the origin of the streaking and splitting of superreflections due to the diffuse scattering along the MRM lines. (a) A reciprocal rod connecting superlattice points $(5\ 3\ \bar{5})/2$ and $(7\ 3\ \bar{5})/2$ is tangential to the Ewald sphere (ES), forming a sharp streak. (b) Two reciprocal rods intersect with the Ewald sphere, forming two splitting spots. Note, the splitting distance is proportional to the deviation of the superlattice point from the Ewald sphere. (c) One reciprocal rod is extinct, and only one spot is visible.

belonging to the three orientational domains V_a, V_b, and V_c that are transformed from the same reciprocal point of the cubic $\mathrm{SrTiO_3}$. Therefore, the three reciprocal rods along the cubic $[1\,0\,0]_p^*$, $[0\,1\,0]_p^*$, and $[0\,0\,1]_p^*$ directions, corresponding to the tetragonal $[0\,0\,1]_T$ directions of the orientational domains V_a, V_b, and V_c, respectively, will pass through a single $(h\,k\,l)/2$ superlattice point if h, k, and l are not equal. If a reciprocal rod is tangential to the Ewald sphere, a streak is observed. This situation is schematically shown in Fig. 5(a) where the reciprocal rod along the $[1\,0\,0]_p^*$ direction passing through the superreflections $(5\,3\,\bar{5})/2$ and $(7\,3\,\bar{5})/2$, is tangential to the Ewald sphere (ES). If two rods originated from a same superlattice point intersect with the Ewald sphere, we would observe two intersection spots whose separation is proportional to the deviation of the superlattice point from the Ewald sphere. Such a situation is schematically shown in Fig. 5(b). Here, two reciprocal rods along the $[0\,1\,0]_p^*$ and $[0\,0\,1]_p^*$ directions pass through each of the superreflections $(7\,\bar{1}\,\bar{1})/2$, $(9\,\bar{1}\,\bar{1})/2$, and $(11\,\bar{1}\,\bar{1})/2$. The deviation from the Ewald sphere of the superlattice point $(7\,\bar{1}\,\bar{1})/2$ is larger than that of point $(9\,\bar{1}\,\bar{1})/2$. Moreover, there is an extinction condition for these rods. For the point $(h\,k\,k)/2$, only two reciprocal rods pass through it, along the $[0\,1\,0]_p^*$ and $[0\,0\,1]_p^*$ directions, belonging to the orientational domains V_b and V_c, respectively, because the structure factor of the corresponding superreflection for the domain V_a is equal to zero. Such a situation is depicted in Figs. 5(a)–5(c), where the extinct reciprocal rods are denoted by dashed lines. The reciprocal rod along the $[1\,0\,0]_p^*$ direction passing through the point $(11\,\bar{1}\,\bar{1})/2$ is extinct [Fig. 5(b)]. Hence, no streak was observed, even though this rod is tangential to the Ewald

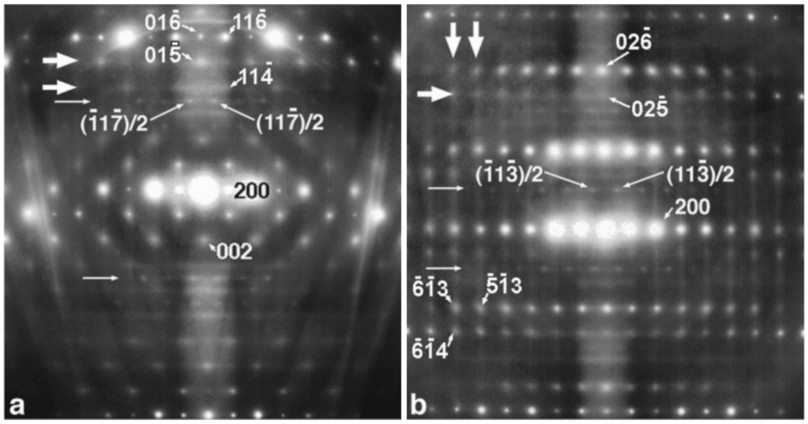

FIG. 6. EDPs at 420 K along different directions between [0 1 0] and [0 1 1] axes, showing diffuse scattering, originated from reciprocal {0 0 1}* sheets, as marked by horizontal and vertical broad arrows. (a) Along the [0 6 1] axis, which deviates by 8.3° from the [0 1 0] axis towards the [0 1 1] direction. (b) Along the [0 3 1] axis, which deviates by 18.5° from the [0 1 0] axis towards the [0 1 1] direction.

sphere. The rods along the $[0\,0\,1]_p^*$ direction, passing through the points $(3\,3\,\bar{5})/2$ and $(\bar{3}\,\bar{3}\,5)/2$ as shown in Figs. 5(a) and 5(c), respectively, have vanished. Hence, we observed only the upper spot of the split $(3\,3\,\bar{5})/2$ reflection, and the lower spot of the split $(\bar{3}\,\bar{3}\,5)/2$ reflection.

The intensity of the ⟨1 0 0⟩* streaks also depends on the geometry of the sample. Usually, streaks are stronger in a thin, buckled area than in a thick, flat area, probably due to local strain. For cubic $SrTiO_3$, the intensity and sharpness of the ⟨1 0 0⟩* streaks decrease with increasing temperature, but are still visible at 500 K. This can be seen by comparing the streak connecting *R* points $(\bar{3}\,\bar{5}\,7)/2$ and $(\bar{1}\,\bar{5}\,7)/2$ in Fig. 2(a) (taken at 20 K), with that in Fig. 2(b) (taken at 422 K), and also comparing the streaks connecting *R* points $(\bar{1}\,9\,\bar{7})/2$ and $(1\,9\,\bar{7})/2$ in Figs. 4(a) (taken at 24 K), and 4(b) (taken at 90 K) with those in Fig. 4(c) (297 K), 4(d) (500 K), and 4(e) (700 K). For tetragonal $SrTiO_3$, these streaks are along the $[0\,0\,1]_T^*$ direction and pass through superlattice points. For cubic $SrTiO_3$, these streaks are along the MRM lines shown in Fig. 1, as described by Shirane,[7] using the conventional notation for reciprocal space of a simple cubic lattice. Such diffuse scattering can be due to the correlated- and uncorrelated-rotation of the TiO_6 octahedra in the (001) layers. We discuss this further in Sec. IV.

B. Diffuse scattering around the *R* points and around the Bragg reflections

In Figs. 2, 3, and 4, all $(h\,k\,l)/2$ reflections with *h*, *k* and *l* being all odd are the *R* points, as shown in Fig. 1, of the cubic $SrTiO_3$ when $T > T_c$ [Figs. 2(b), 4(c), 4(d), and 4(e)]. They are superreflections of the tetragonal $SrTiO_3$ when $T < T_c$ [Figs. 2(a), 3, 4(a), and 4(b)]. These spots are sharp and strong in Fig. 2(a) (taken at 20 K), Fig. 3 (at 20 K), Fig. 4(a) (at 24 K), and Fig. 4(b) (at 90 K), but become weaker and broader when the temperature is increased [Figs. 2(b), 4(c), 4(d), and 4(e)]. However, they remain visible [Fig. 4(e)] at $T = 700\,\mathrm{K}$.

The intensity of thermal diffuse-scattering around a Bragg reflection is nearly proportional to the integrated intensity of the Bragg reflection, and inversely proportional to the square of the modulus of the wave vector of the relevant phonons. Due to thermal diffuse scattering, we observe broad diffuse spots at the positions where the relevant reflections do not fulfill the Bragg condition, for example, the broad diffuse spots at the (2 0 0) and $(3\,0\,\bar{1})$ reflection positions in Fig. 2(b), and those at the $(0\,3\,\bar{3})$ and $(1\,3\,\bar{2})$ reflection positions in Fig. 4(e).

Figures 6(a) and 6(b) are EDPs taken at 420 K. The EDP in Fig. 6(a) deviates by 8.3° from the [0 1 0] axis towards the [0 1 1] direction, and the one in Fig. 6(b) is along the [0 3 1] axis and deviates by 18.5° from the [0 1 0] axis towards the [0 1 1] direction. The three types of diffuse scattering discussed above are evident: Diffuse scattering around the *R* points, such as $(\bar{1}\,1\,\bar{7})/2$ and $(1\,1\,\bar{7})/2$ in Fig. 6(a), and $(\bar{1}\,1\,\bar{3})/2$ and $(1\,1\,\bar{3})/2$ in Fig. 6(b); Thermal diffuse-scattering around Bragg reflections, such as spots $(0\,1\,\bar{5})$, $(1\,1\,\bar{4})$, and $(0\,2\,\bar{5})$; and Diffuse scattering along the MRM line, that is, the $[1\,0\,0]^*$ streaks passing through the *R* points marked by horizontal thin arrows. The third type of diffuse scattering was described in detail in Sec. III A. The diffuse scattering around the *R* point is due to the Γ_{25} mode, as reported in the neutron diffraction study[1] (also see Sec. IV).

C. Diffuse scattering of {0 0 1}* reciprocal sheets passing through fundamental reflections

We observe another type of diffuse scattering that runs through fundamental reflections and is perpendicular to ⟨1 0 0⟩ directions, as denoted by broad arrows in Fig. 6. For example, strong horizontal lines of diffuse scattering pass through fundamental reflections $(0\,1\,\bar{5})$, $(1\,1\,\bar{4})$, and $(0\,2\,\bar{5})$, which deviate from the Bragg condition, as indicated by the horizontal broad arrows in Figs. 6(a) and 6(b). However, there are no discernible horizontal lines of diffuse scattering passing through fundamental reflections $(1\,1\,\bar{6})$ and $(0\,2\,\bar{6})$, which nearly fulfill Bragg condition. In addition, we observed strong vertical lines of diffuse scattering passing through fundamental reflections, e.g., $(\bar{6}\,\bar{1}\,3)$ and $(\bar{5}\,\bar{1}\,3)$, which also deviate from Bragg condition, as indicated by the vertical broad arrows in Fig. 6(b). The intensity of the vertical lines of diffuse scattering decreases with the perpendicular distance of the lines to the (0 0 0) spot of the EDP, and no vertical line passes through the origin of the EDP. Such diffuse scattering also were observed when the crystal was tilted away from the ⟨0 1 0⟩ axis. For the EDP at the exact ⟨0 1 0⟩ orientation, such diffuse scattering was not

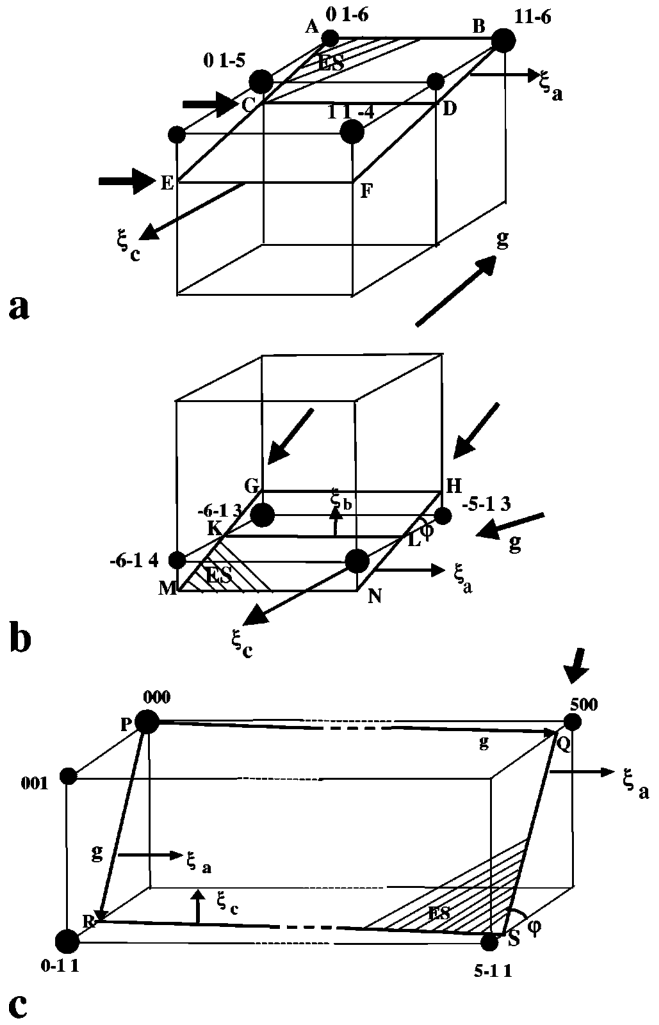

FIG. 7. Schematic diagrams showing the formation of the diffuse intensity caused by the reciprocal {0 0 1}* sheets. The intensity of the diffuse scattering is proportional to the value of $(\mathbf{g}\cdot\xi)^2 \sin\varphi$. When the value is large, strong diffuse scattering is observed corresponding to the lines CD and EF in (a), GM and HN in (b), and QS in (c), as pointed by broad arrows. No diffuse intensity along the ΓX line (see Fig. 1), i.e., the lines *AB* in (a) and *PQ* in (c) because ξ is zero. When **g** is nearly perpendicular to ξ, i.e., lines *AE* and *BF* in (a), *KL* in (b), and *PR* in (c), no diffuse intensity is observed. A small glancing angle φ decreases the diffuse intensity by a factor of $\sin\varphi$, as for the line *KL* in (b) and *RS* in (c).

observed in the zeroth-order Laue zone (ZOLZ) of the EDP, but was visible in the region between ZOZL and FOLZ (first-order Laue zone).

In Fig. 4(e), a line of diffuse scattering perpendicular to the [2 0 0] direction and passes through fundamental reflections, as pointed by a vertical broad arrow, and then passes through the $(5\,\bar{1}\,1)$ spot. Such diffuse scattering was seen readily when the crystal was tilted away from the ⟨0 1 1⟩ axis, as pointed by the broad arrows in Fig. 2(b).

Systematic tilting experiments (from the [0 1 0] zone to the [0 1 1] zone, to the [1 2 1] zone, and then to the [0 1 0] zone) reveal that the diffuse scatterings originate from the (0 0 1)* reciprocal sheets passing through the reciprocal lattice points. Noticing[10–12] that the intensity of the diffuse scattering is proportional to $|F(\mathbf{g})|^2(\mathbf{g}\cdot\xi)^2$, with $F(\mathbf{g})$ being the structure factor of the reflection **g** and ξ the polarization vector of the related phonon, all the observed relative intensities of such diffuse scatterings may be interpreted by assuming that ξ is perpendicular to each sheet, except near the ΓX line which is an intersection of two perpendicular (0 0 1)* sheets. Along the ΓX line, ξ is zero. Figure 7 explains some of these observations. In Fig. 7(a), the Ewald sphere (ES) nearly intersects the reciprocal points $(0\,1\,\bar{6})$ and $(1\,1\,\bar{6})$; its intersections with the {0 0 1}* sheets are lines *AB*, *CD*, *EF*, *AE*, and *BF*. Among them, the polarization vector ξ_c relevant to *CD* and *EF* is parallel to the [0 0 1] direction with a larger value of $(\mathbf{g}\cdot\xi)^2$, resulting in stronger diffuse scattering, as indicated by two horizontal broad arrows in Figs. 6(a) and 7(a). However, the polarization vector ξ relevant to *AB* is zero, and the polarization vector ξ_a relevant to *AE* and *BF* is parallel to the [1 0 0] direction with a nearly zero $(\mathbf{g}\cdot\xi)^2$ value; hence, no diffuse scattering is observed. In Fig. 7(b), the intersections of the Ewald sphere with the {0 0 1}* sheets are lines *GH*, *KL*, *MN*, *GM*, and *HN*. Among them the polarization vector ξ_a relevant to *GM* and *HN* is parallel to the [1 0 0] direction with a large value of $(\mathbf{g}\cdot\xi)^2$, and hence, stronger diffuse scatterings form, as indicated by two vertical broad arrows in Figs. 6(b) and 7(b). The polarization vector ξ_c relevant to *GH* and *MN* is parallel to the [0 0 1] direction with smaller value of $(\mathbf{g}\cdot\xi)^2$, and hence, very weak diffuse scattering is observed. The polarization vector ξ_b relevant to *KL* is parallel to the [0 1 0] direction with very small value of $(\mathbf{g}\cdot\xi)^2$. Moreover, the glancing angle, φ, between the Ewald sphere and the diffuse intensity sheet is small. Therefore, the width of the diffuse line is increased by a factor of $1/\sin\varphi$, and its diffuse intensity is correspondingly decreased by a factor of $\sin\varphi$, and thus is invisible. In Fig. 7(c), the intersections of the Ewald sphere with the {0 0 1}* sheets are lines *PQ*, *RS*, *PR*, and *QS*. Among them, the polarization vector ξ_a relevant to *PR* and *QS* is parallel to the [1 0 0] direction. The strong intensity of line *QS* is due to its large value of $(\mathbf{g}\cdot\xi)^2$, as marked by a vertical broad arrow in Figs. 4(e) and 7(c) Line *PR* has a zero value of $(\mathbf{g}\cdot\xi)^2$. The polarization vector ξ_c relevant to the line *RS* is parallel to the [0 0 1] direction with small values of $(\mathbf{g}\cdot\xi)^2$. The glancing angle φ relevant to the line *RS* is about 45°, thereby spreading the intensity of diffuse scattering into a large area. The polarization vector ξ of the line *PQ* is nearly zero; thus, there is no discernible diffuse scattering corresponding to lines *PR*, *PQ*, and *RS*. The intensity of such diffuse scattering increases with temperature, and is even visible in its tetragonal form [Fig. 4(b)]. The origin of the {001}* diffuse sheet is discussed in Sec. IV.

D. Correlation lengths of dynamic oscillations of soft phonons at room temperature

To obtain the correlation lengths of the dynamic oscillations of the observed soft phonons, we measured the values of the full width at half maximum (FWHM) of the line profiles of some diffuse scatterings. Figure 8(a) is an EDP near the [001] axis at *RT* (deviates from the [0 0 1] axis by 9° towards the $[\bar{1}\,\bar{1}\,1]$ direction), showing the four types of diffuse scattering discussed above: (a) Diffuse scattering around the *R* points, such as (7 1 1)/2 and $(7\,\bar{1}\,1)/2$ boxed in Fig. 8(a), 8(b) diffuse scattering along the *RM* line, such as the streak connecting the *R* points (7 1 1)/2 (R_1) and

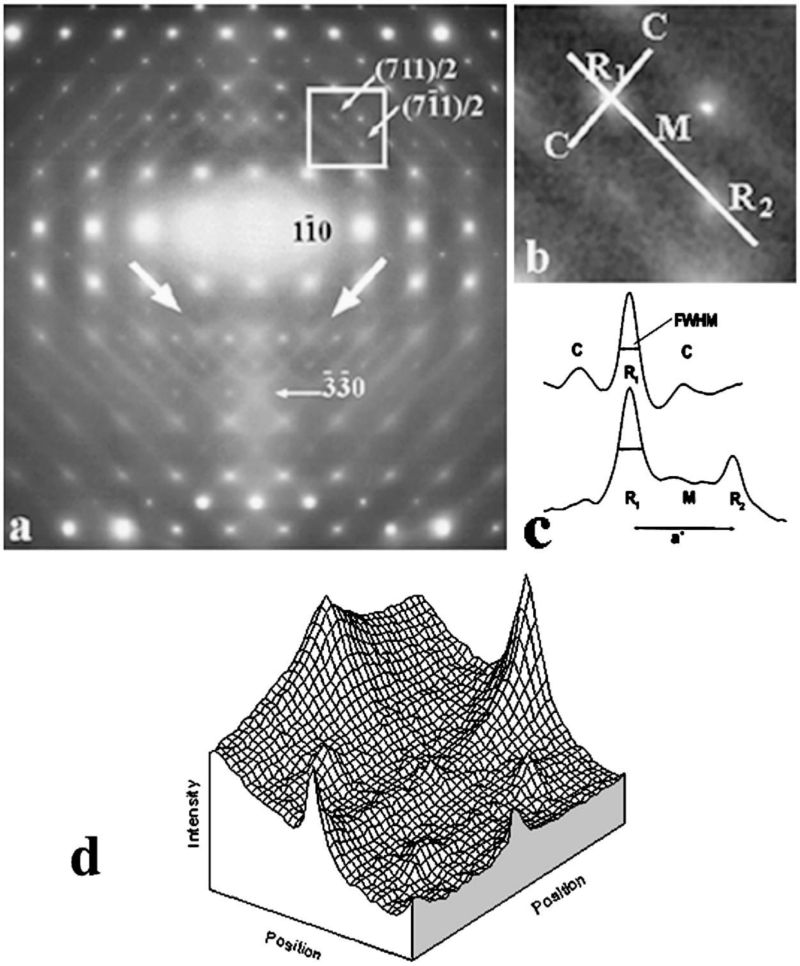

FIG. 8. (a) EDP at RT, which deviates from the [0 0 1] axis by 9° towards the $[\bar{1}\,\bar{1}\,1]$ direction. (b) the enlarged boxed area in (a), showing R points at the positions of (7 1 1)/2 and $(7\,\bar{1}\,1)/2$, and the streak connecting them. (c) Line profiles CR_1C and R_1MR_2. CR_1C crosses the spot R_1 and R_1MR_2 crosses spots (7 1 1)/2 (R_1) and $(7\,\bar{1}\,1)/2\,(R_2)$. FWHM denotes the full width at half maximum of the intensity peak. (d) A surface plot of the diffuse scatterings from an area near the $(\bar{3}\,\bar{3}\,0)$ reflection, showing the intensity distribution of all four types of diffuse scatterings.

$(7\,\bar{1}\,1)/2\,(R_2)$ [Fig. 8(b), enlarged boxed area in (a)], (c) Thermal diffuse scattering around the Bragg reflections, such as the spot $(\bar{3}\,\bar{3}\,0)$, (d) Diffuse scattering originating from reciprocal {0 0 1}* sheets passing through fundamental spots, such as those indicated by broad arrows. A surface plot of the diffuse scatterings, as shown in Fig. 8(d) from an area near $(\bar{3}\,\bar{3}\,0)$ reflection in Fig. 8(a), clearly visualizes the intensity distribution with streaks of diffuse scattering of the four types. The four closed squares are formed by the {001}* sheets with a R point sitting in the middle of each square. The intensities connecting the R points are the [001]* rods. We note the fall off of the intensity from left to right due to the unsubtracted background. Figure 8(c) shows two line-profiles crossing the spot (711)/2 (R_1), and crossing the spots (711)/2 and $(7\,\bar{1}\,1)/2\,(R_2)$, as marked in Fig. 8(b). The points C and M denote the intersection positions of the {001}* sheets and [001]* rods. Measurements showed the values of the FWHM of the peaks R_1 and R_2 were equal to $0.222a^*$, where a^* is the length of the reciprocal vector of the cubic $\mathrm{SrTiO_3}$. This corresponds to an inverse correlation length of $\kappa[001]/2\pi a^* = 0.111$, and suggests a correlation length of about nine perovskite unit-cells $(\zeta_R = 9a_p)$ for the dynamic rotation of the octahedra around ⟨1 0 0⟩ axis of the Γ_{25} soft phonon at RT.

Figure 9(a) shows an EDP at RT recorded with a digital slow-scan CCD camera. The zone axis deviates from the [0 1 0] axis by 11° towards the [0 1 1] direction. The strong diffuse scattering of the projected {001}* sheets perpendicular to [1 0 0]* direction are indicated by vertical broad arrows, and those perpendicular to [0 0 1] direction by horizontal broad arrows. Line profiles NN' and EE' are shown in Fig. 9(b), where NN' crosses two vertical diffuse sheets passing through spots $(\bar{6}\,0\,0)$ and $(\bar{4}\,0\,0)$, and EE' crosses two horizontal diffuse sheets passing through spots (0 0 4) and (0 0 2). The values of the FWHM of the peaks are equal to $0.36a^*$, suggesting a correlation length of $\zeta_S = 5.5a_p$ for

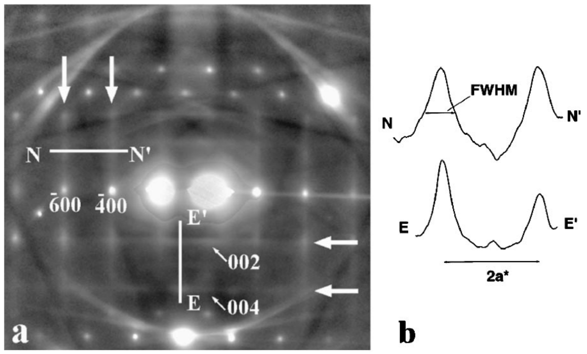

FIG. 9. (a) EDP at RT, which deviates from the [0 1 0] axis by 11° towards the [0 1 1] direction. (b) Line profiles NN' and EE'. NN' crosses two diffuse sheets which pass through spots $(\bar{6}\,0\,0)$ and $(\bar{4}\,0\,0)$. EE' crosses two diffuse sheets which pass through spots (0 0 4) and (0 0 2). FWHM, denoted the full-width-at-half-maximum of each peak, is about $0.36a^*$ for both peaks. Note, the EE' line passes an R point.

the dynamic movement of the atoms of the relevant soft phonon at RT.

IV. DISCUSSION

Among the diffuse scatterings described in Sec. III, thermal diffuse scattering around Bragg reflections is well known. Our observations are (1) streaks of diffuse scattering along the MRM lines. Their intensity is very strong for tetragonal $SrTiO_3$ and decreases with increasing temperature, especially at $T > 103\,K$ (cubic $SrTiO_3$). (2) Diffuse scattering around the R point, which becomes a superlattice point of the tetragonal $SrTiO_3$ when $T < T_c$. Its intensity also decreases with the increase of temperature, but it is visible even at $T = 700\,K$. (3) Diffuse scattering of the X-Γ-X-M-X sheets, which are reciprocal $\{001\}^*$ planes passing through fundamental lattice points. The polarization vector ξ of the related phonon is perpendicular to the sheet, except in the vicinity of the ΓX line where ξ is zero.

As Glazer[11] pointed out, successive TiO_6 octahedra in the *a-b* plane are constrained to rotate around the [0 0 1] axis in an opposite sense (correlated rotations), while successive octahedra along the rotation axis can have either the same or the opposite sense of rotation. Noticing the observed reciprocal rods along $\langle 1\ 0\ 0\rangle^*$ direction passing through superreflections of the tetragonal $SrTiO_3$ and their extinction conditions, we propose a structural model of the anti-phase domains within each orientational variant of the tetragonal $SrTiO_3$. In our model, each orientational variant is stacked by very thin plates of domains parallel to the tetragonal *a-b* plane, and the translation vector between two neighbouring plates is $\langle 1/2\ 0\ 0\rangle$ when a tetragonal cell with an edge length of $2a_p$ is used (Fig. 10(a)). This translation vector is exactly the same as the one lost when the cubic $SrTiO_3$ of the space group $Pm\bar{3}m$ is transformed into the tetragonal $SrTiO_3$ of the space group $F4/mmc$. Such a model of the anti-phase domains can also be described as one in which the successive TiO_6 octahedra in a same anti-phase domain rotate in opposite sense, while the successive octahedra lying at different sides of the anti-phase domain boundary (*APB*) rotate in the same sense.

Similarly, the streaks of diffuse scattering along the *MRM* lines in cubic $SrTiO_3$ may be interpreted as a dynamic rotation of oxygen-octahedra, with the rotations about the [0 0 1] axis of octahedra in each (0 0 1) layer correlated, while they are uncorrelated between layers. This configuration means that successive TiO_6 octahedra in the *a-b* plane are constrained to rotate in opposite sense, while successive octahedra along the rotation axis can have either the same or the opposite sense of rotation. When temperature decreases, such dynamic rotation becomes intensified relative to other thermal vibrations. This interpretation is consistent with the Stirling's neutron inelastic scattering study[12] in which the frequency of the entire *MR* branch decreased with temperature (from 297 K to 78 K). When the temperature is lowered to T_c, such a dynamic rotation condenses into thin plates of anti-phase domains. Hence, the present work reveals that condensations of soft phonons may lead not only to phase transition, but also to the formation of a localized microstructure.

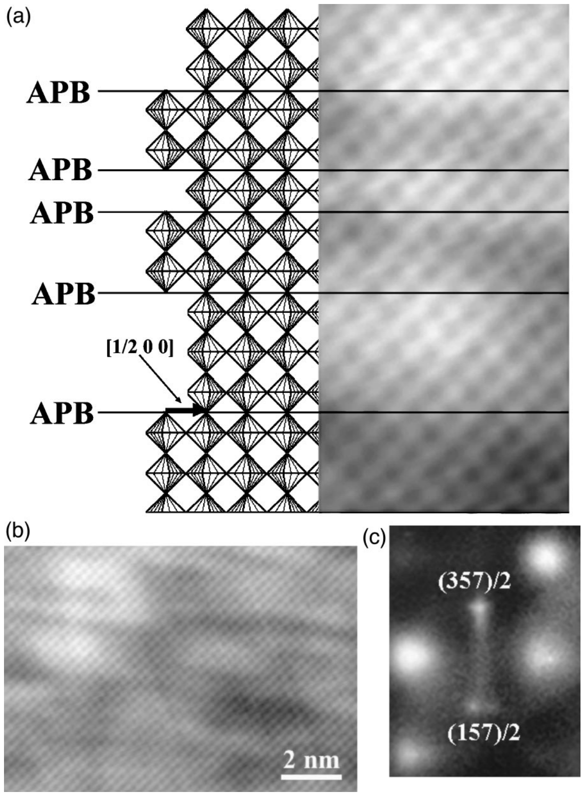

FIG. 10. (a) Left: structural model of the antiphase domains in the tetragonal $SrTiO_3$. Each orientational variant consists of very thin plates of domains, parallel to the *a-b* plane, and stacked along the *c* axis. The translation vector between two neighboring plates is $\langle 1/2\ 0\ 0\rangle$, using $2a_p$ as the edge length of the unit cell. Right: [010] projection of a high-resolution image of $SrTiO_3$, showing black dots as Sr/O columns and white dots as Ti/O columns. Note, the black and white bands are antiphase domains with their interfaces as antiphase boundaries running parallel to the *a* axis. (b) High-resolution image from a larger area similar to that in (a). (c) Corresponding diffraction pattern of (b), showing a diffuse streak perpendicular to the antiphase boundaries.

Fig. 10(a) is a sketch of the model along with an experimental HREM image of the $SrTiO_3$ on its right. The image is viewed along the [010] direction with Sr and O atom columns appearing black dots, while Ti and O atom columns as white dots. The white-black band-contrast running along the [100] direction results from the rotation of the TiO_6 octahedra; the interfaces between the black-white bands are the antiphase boundaries. Figure 10(b) shows a larger area of antiphase domains and domain boundaries. Figure 10(c) is the diffuse scattering of the corresponding area, showing a streak of diffuse scattering perpendicular to the elongated anti-phase domain and their interfaces. The experimental diffraction and high-resolution images are consistent with our structural model.

Comes *et al.*[13] observed x-ray diffuse scattering along $[1\ 0\ 0]^*$ reciprocal rods, passing through R points, in cubic $KMnF_3$ single crystal. They explained their observations in terms of correlated rotations of the fluorine octahedra in a same (1 0 0) plane, and uncorrelated rotations from one (1 0 0) layer to another. This interpretation is the same as that we have suggested above, for cubic $SrTiO_3$. Gesi *et al.*[14] measured the dispersion curves of $KMnF_3$ by neutron inelastic scattering and found a soft, nearly flat branch from R to M

at RT. This suggests that the observed x-ray diffuse scattering along *RM* rods in cubic KMnF$_3$ crystal is caused by soft phonons, and hence, the correlated and uncorrelated rotations of the fluorine octahedra in cubic KMnF$_3$ are dynamic. Recently, using high-energy monochromatic Laue x-ray scattering with imaging plates, Gibaud *et al.*[15] observed some intensity along the entire length of the *RM* line of the cubic KMnF$_3$. However, with decreasing temperature, such soft phonons in cubic SrTiO$_3$ condense into thin plates of antiphase domains of tetragonal SrTiO$_3$. Such a microstructure exists when temperature falls to 20 K. For KMnF$_3$, such soft phonon condensation occurs first at the *R* point at 186.5 K, then at the *M* point at 90 K; the diffuse intensity along the *RM* line suddenly disappears when the temperature falls further.[15]

Diffuse scattering around the *R* point is known to be due to the Γ_{25} phonon mode; its instability causes the cubic-to-tetragonal phase transition of SrTiO$_3$ at $T_c \simeq 103\,\mathrm{K}$. Due to the high sensitivity of electron diffraction in detecting a very weak diffraction intensities, we observed diffuse scattering around the *R* point at very high temperature ($T = 700\,\mathrm{K}$). Otnes *et al.*[3] studied the high-temperature behavior (300–900 K) of the Γ_{25} soft mode by inelastic neutron scattering. They found that the energy of the Γ_{25} mode increases with the temperature nearly according to the Curie-Weiss law, but the energy value at 900 K ($\sim$12 meV) is still lower than the maximum value ($\sim$15 meV) of the lowest phonon branch along the ΓR line, as measured by Shirane and Yamada.[1] This implies that the diffuse scattering around the *R* point at high temperature, observed in the present work, is caused by soft phonons.

The temperature dependence of the inverse correlation length κ follows a power law $\kappa[110]/2\pi a^* = 0.0849\,t^{0.83}$, where t is the reduced temperature, $t = (T - T_c)/T_c$.[4] Extending this power law to $\mathrm{RT} = 293\,\mathrm{K}$, we obtain $\kappa[110]/2\pi a^* = 0.1413$ for the [1 1 0] direction. Since McMorrow *et al.*[5] and Hirota *et al.*[5] found that $\kappa[110]$ is $\sim$36% larger than $\kappa[001]$, we calculated $\kappa[001]/2\pi a^* = 0.104$. Considering the value of $\kappa[001]/2\pi a^* = 0.111$, as discussed in Sec. III D, is the experimental measurement of raw data without deconvolution of the instrumental widening, the agreement with the power law is good.

The cubic-tetragonal phase transition is induced by condensation of the Γ_{25} phonon mode. At high temperature, $\kappa[100]$ is large, i.e., the correlation length ζ is small. Here, ζ is a direct measure of the size of domains in which the local structure is instantaneously tetragonal. The domain size increases as the temperature is reduced. When the temperature T reaches the transition temperature T_c, the domain size ζ becomes infinite. The wntire crystal transforms into a new tetragonal phase.

As Honjo *et al.*[16] and Comes and Shirane[17] reported BaTiO$_3$, KNbO$_3$, and KTaO$_3$ all show strong diffuse scattering of the {0 0 1}* reciprocal sheets. Our electron diffraction study revealed a weak diffuse scattering of the reciprocal {0 0 1}* sheets in SrTiO$_3$, which we attributed to the correlated movements along the [0 0 1] direction of the atoms which form atomic chains along the [0 0 1] direction, similar to that proposed by Comes and Shirane for KTaO$_3$.[17] As shown in Fig. 11, the successive Ti^{+4}-O^{2}-Ti^{+4} chain of positive and negative ions and the shortest Ti^{+4}-Ti^{+4} bonding distance along the [0 0 1] direction favor the correlated displacements of the ions along the c axis.

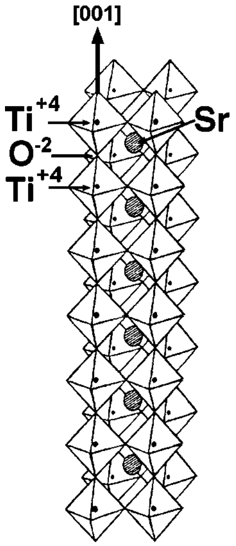

FIG. 11. Correlated movements of the ions forming successive Ti^{+4}-O^{-2}-Ti^{+4} chains along the [0 0 1] direction. A one-dimensional correlation leads to the diffuse scattering of the {0 0 1}* reciprocal sheets in SrTiO$_3$.

The behavior of the soft phonons and the associated phase transitions in *ABX*$_3$ perovskites seems to be related to the tolerance factor $\tau = (r_A + r_X)/\sqrt{2}(r_B + r_X)$ where r_A, r_B, and r_X are the ion radii of the *A*, *B*, and *X* ions, respectively, as summarized by Shannon.[18] The tolerance factor τ describes the size of the octahedra consisting of the *X* ions relative to that of the *B* ions. We calculated the values of τ for BaTiO$_3$, KNbO$_3$, KTaO$_3$, SrTiO$_3$, KMnF$_3$, KCaF$_3$, and CsPbCl$_3$; they are 1.058, 1.050, 1.050, 0.999, 0.978, 0.905, and 0.869, respectively. When $\tau = 1.000$, all the ions touch each other and the cubic perovskite is stable. As pointed out by Gibaud *et al.*[19] perovskites that have a small τ factor, for example, KCaF$_3$ and CsPbCl$_3$, seem to display the *M*-point transition first at relatively high temperatures, and then the *R*-point transition. For KMnF$_3$, whose τ value ($\tau = 0.978$) is close to but less than 1, the *R*-point transition occurs first and then the *M*-point transition. The τ factor for SrTiO$_3$ is nearly equal to 1 and hence the *M*-point transition is further suppressed. Therefore, SrTiO$_3$ perovskite displays strong diffuse intensity along the *MRM* line down to a very low temperature (20 K). On the other hand, perovskites having a τ factor larger than 1, e.g., BaTiO$_3$ and KNbO$_3$, display ferroelectric transition[20] and strong diffuse intensity in the {0 0 1}* sheets.[16,17] Furthermore, the larger the space available for the *B* ions, the stronger are the correlated movements of the ⟨0 0 1⟩ atomic chains, and hence, the more diffuse scattering in the reciprocal {0 0 1}* sheets. SrTiO$_3$ has a smaller τ factor than BaTiO$_3$, KNbO$_3$, and KTaO$_3$, and accordingly, weaker diffuse intensity in {0 0 1}* sheets.

In summary, we observed three types of diffuse scattering associated with phonon and static disorder in SrTiO$_3$ using selected-area electron diffraction. The diffuse scattering around the *R* point originated from the Γ_{25} phonon mode, the [001]* streaks of diffuse scattering are due to dynamic correlated rotations of oxygen-octahedra within the *a*-*b* plane, while the (001)* sheets of diffuse scattering are due to the correlated movements of atomic chains along the *c*-direction. The correlation length of the dynamic oscillations of the soft phonons at room temperature was also discussed.

ACKNOWLEDGMENTS

This work is supported by the U.S. Department of Energy, Division of Materials Sciences, Office of Basic Energy Sciences under Contract No. DE-AC02-98CH10886.

---

*Author to whom correspondence should be addressed. Present address: Bldg. 480, Brookhaven National Laboratory, Upton, NY 11973-5000. Electronic address: zhu@bnl.gov FAX: 631-344-4071.

[1] G. Shirane and Y. Yamada, Phys. Rev. **177**, 858 (1969).

[2] S. M. Shapiro, J. D. Axe, G. Shirane, and T. Riste, Phys. Rev. B **6**, 4332 (1972).

[3] K. ’Otnes, T. Riste, G. Shirane, and J. Feder, Solid State Commun. **9**, 1103 (1971).

[4] S. R. Andrews, J. Phys. C **19**, 3721 (1986).

[5] D. F. McMorrow, N. Hamaya, S. Shimomura, Y. Fujii, S. Kishimoto, and H. Iwasaki, Solid State Commun. **76**, 443 (1990); K. Hirota, J. P. Hill, S. M. Shapiro, G. Shirane, and Y. Fujii, Phys. Rev. B **52**, 13 195 (1995).

[6] H. Fujishita, Y. Shiozaki, and E. Sawaguchi, J. Phys. Soc. Jpn. **46**, 581 (1979).

[7] G. Shirane, Rev. Mod. Phys. **46**, 437 (1974).

[8] K. Tsuda and M. Tanaka, Acta Crystallogr., Sect. A: Found. Crystallogr. **51**, 7 (1995).

[9] *International Tables for Crystallography, Vol. A, Space-Group Symmetry*, edited by T. Hahn (Reidel, Dordrecht, 1983).

[10] Y. Zhu and J. M. Cowley, Philos. Mag. A **69**, 397 (1994).

[11] A. M. Glazer, Acta Crystallogr., Sect. B: Struct. Crystallogr. Cryst. Chem. **28**, 3384 (1972).

[12] W. G. Stirling, J. Phys. C **5**, 2711 (1972).

[13] R. Comes, F. Denoyer, L. Deschamps, and M. Lambert, Phys. Lett. **34A**, 65 (1971).

[14] K. Gesi, J. D. Axe, G. Shirane, and A. Linz, Phys. Rev. B **5**, 1933 (1972).

[15] A. Gibaud, D. Harlow, J. B. Hastings, J. P. Hill, and D. Chapman, J. Appl. Crystallogr. **30**, 16 (1997).

[16] G. Honjo, S. Kodera, and N. Kitamura, J. Phys. Soc. Jpn. **19**, 351 (1964).

[17] R. Comes and G. Shirane, Phys. Rev. B **5**, 1886 (1972).

[18] R. Shannon, Acta Crystallogr., Sect. A: Cryst. Phys., Diffr., Theor. Gen. Crystallogr. **32**, 751 (1976).

[19] A. Gibaud, S. M. Shapiro, J. Nouet, and H. You, Phys. Rev. B **44**, 2437 (1991).

[20] W. Zhong and D. Vanderbilt, Phys. Rev. Lett. **74**, 2587 (1995).